"Hybrid Ligand Exchange of $Cu(In,Ga)S_2$ Nanoparticles for Carbon Impurity Removal in Solution-Processed Photovoltaics" was published in *Chemistry of Materials* on May 5, 2020.

Ellis, R. G.*, Turnley, J. W.*, Rokke, D. J.*, Fields, J. P., Alruqobah, E. H., Deshmukh, S. D., Kisslinger, K., & Agrawal, R. (May, 2020). Hybrid Ligand Exchange of $Cu(In,Ga)S_2$ Nanoparticles for Carbon Impurity Removal in Solution-Processed Photovoltaics. *Chemistry of Materials, 32*, 12, 5091–5103. https://dx.doi.org/10.1021/acs.chemmater.0c00966?ref=pdf.

Hybrid Ligand Exchange of $Cu(In,Ga)S_2$ Nanoparticles for Carbon Impurity Removal in Solution Processed Photovoltaics

Ryan G. Ellis, Jonathan W. Turnley, David J. Rokke, Jacob P. Fields, Essam H. AlRuqobah, Swapnil D. Deshmukh, Kim Kisslinger [‡] and Rakesh Agrawal*

Davidson School of Chemical Engineering, Purdue University, West Lafayette, IN 47907, USA
[‡] Center for Functional Nanomaterials, Brookhaven National Laboratory, Upton, NY 11973, USA

*Corresponding Author: agrawalr@purdue.edu

Abstract

The solution processing of $Cu(In,Ga)(S,Se)_2$ photovoltaics from colloidal nanoparticles has long suffered from deleterious carbonaceous residues originating from long chain native ligands. This impurity carbon has been observed to hinder grain formation during selenization and leave a discrete residue layer between the absorber layer and the back contact. In this work, organic and inorganic ligand exchanges were investigated to remove tightly bound native oleylamine ligands from $Cu(In,Ga)S_2$ nanoparticles, thereby removing the source of carbon contamination. However, incomplete ligand removal, poor colloidal stability, and/or selective metal etching was observed for these methods. As such, an exhaustive hybrid organic/inorganic ligand exchange was developed to bypass the limitations of individual methods. A combination of microwave-assisted solvothermal pyridine ligand stripping followed by inorganic capping with diammonium sulfide was developed and yielded greater than 98% removal of native ligands via a rapid process. Despite the aggressive ligand removal, the nanoparticle stoichiometry remained largely unaffected when making use of the hybrid ligand exchange. Furthermore, highly stable colloidal ink formulations using non-toxic dimethyl sulfoxide were developed, supporting stable nanoparticle mass concentrations exceeding 200 mg/mL. Scalable blade coating of the ligand exchanged nanoparticle inks yielded remarkably smooth and microcrack free films with RMS roughness less than 7 nm. Selenization of ligand exchanged nanoparticle films afforded substantially improved grain growth as compared to conventional non-ligand exchanged methods yielding an absolute improvement in device efficiency of 2.8%. Hybrid ligand exchange nanoparticle based devices reached total-area power conversion efficiencies of 12.0%, demonstrating the feasibility and promise of ligand exchanged colloidal nanoparticles for the solution processing of $Cu(In,Ga)(S,Se)_2$ photovoltaics.

Introduction

Solution processing of thin-film photovoltaics has emerged as a promising fabrication technique with the potential to significantly reduce manufacturing costs as compared to traditional vacuum processing. Solution processing offers substantial advantages over high-vacuum batch processing due to its compatibility with atmospheric-pressure, high-throughput, and high-materials-utilization deposition techniques such as slot-die printing, inkjet printing, and blade coating. Of commercial thin-film materials, solution processing of $Cu(In,Ga)(S,Se)_2$ (CIGSSe) absorbers have shown noteworthy promise, reaching certified power conversion efficiencies of 17.3% via a hydrazine based molecular precursor approach.[1] Hydrazine processing is advantageous in that it can solubilize metal, chalcogen, and metal chalcogenides, while also cleanly decomposing under mild thermal treatment. However, due to the explosive and extremely toxic properties of hydrazine, wide-scale deployment of this technology has been hindered by safety concerns. A variety of non-hydrazine molecular precursors and colloidal nanoparticle based approaches to solution processed CIGSSe have emerged as more benign alternatives, where a solution deposited precursor layer is selenized to yield a device-quality film. Similar to hydrazine, mixtures of alkylamines and alkylthiols have demonstrated the ability to solubilize a wide variety of metal salts,[2–6] pure metals,[7–9] chalcogens,[10,11] and metal chalcogenides.[12] Devices fabricated using the amine-thiol molecular precursor approach have reached power conversion efficiencies up to 13.12%.[12] Alternatively, an approach making use of metal chlorides and thiourea in dimethyl sulfoxide[13] (DMSO) or dimethyl formamide[14] (DMF) has reached a champion total-area efficiency of 13.6% (15.2% active area).[15] While the molecular precursor approach is advantageous in its simplicity of ink preparation, the highest efficiency non-hydrazine solution processed device has been achieved through a colloidal nanoparticle approach, reaching a champion power

conversion efficiency of 15% (total-area).[16] While the colloidal nanoparticle approach has added complexity of synthesis over molecular precursors, it has several advantages such as the ability to prepare high mass concentration inks at or above 250 mg/mL allowing compatibility with blade coating and slot die printing. Additionally, at these high mass concentrations, single pass coatings exceeding 800 nm are feasible by highly scalable techniques such as slot-die printing, reducing the number of coating steps substantially as compared to techniques such as spin coating.[17] Furthermore, a wide variety of non-polar solvents can be employed such as hexanethiol, toluene, chlorobenzene, and dichlorobenzene, affording versatility in processing.[16–19]

Despite these benefits, colloidal nanoparticle based photovoltaics have continually suffered from carbonaceous impurity residues that could increase series resistance and recombination, potentially limiting efficiency. These carbonaceous residues originate from long chain organic ligands bound to the surface of the nanoparticles.[20,21] Virtually all common synthetic pathways for chalcogenide nanocrystals make use of low-volatility coordinating ligands that consist of a polar head group to coordinate with the nanocrystal surface, and a long alkyl chain tail to afford colloidal stability via steric repulsion between nanoparticles. Commonly used ligands during colloidal synthesis include oleylamine (OLA, b.p 348-350°C), dodecanethiol (DDT, b.p 266-283°C), trioctylphosphine (TOP, b.p. 284-291°C), and oleic acid (OA, b.p. 360°C).[22,23] These long chain surfactant-like molecules are used during synthesis for their high boiling point, ability to solubilize precursors, and ability to control reaction kinetics and nanoparticle morphology. However, due to the high boiling point of these molecules, they are difficult to remove via thermal treatment and can leave coke residues in the nanoparticle film when annealed under an inert atmosphere.[20] In the case of solution processed CIGSSe and $Cu_2ZnSn(S,Se)_4$ (CZTSSe) photovoltaics from colloidal nanoparticle inks, these ligands decompose and react with a liquid front of selenium during the selenization process. The liquid selenium front segregates a polymeric carbon/selenium fine grain layer to the back contact.[19,24] While this layer is fairly conductive, it still has several orders of magnitude higher resistance than the molybdenum back contact and thereby may increase series resistance.[3,25] Additionally, it has been suggested that the presence of carbon can detrimentally impact the elemental redistribution process that occurs during selenization.[21]

Naturally, removal of these bulky ligands would prevent carbon residues from contaminating nanoparticle thin films. However, due to the benefits of these ligands during nanoparticle synthesis, their removal is preferred post nanoparticle synthesis via ligand exchange reactions. A significant body of literature has explored ligand exchange for metal and metal chalcogenide nanomaterials. Binary materials such as CdSe, CdTe, and PbS have been studied extensively due to their well-defined surface chemistry and application in quantum dot based devices.[26] Their native ligands have been replaced using a wide variety of organics such as pyridine,[27–29] butylamine,[30] ethylenediamine,[31] ethanedithiol,[32] tert-butylthiol,[33] benzenedithiol, 3-mercaptopropionic acid, benzenthiol,[26] and many others. Additionally, inorganic ligands such as hydrazine,[34] diammonium sulfide (DAS), sodium sulfide, sodium azide,[35] ammonium thiocyanate,[34] as well as molecular metal chalcogenide complexes (MCCs) have emerged as promising ligands.[34] These inorganic ligands can be advantageous in that ligands can be selected without impurity elements such as carbon while simultaneously retaining colloidal stability via electrostatic repulsion between nanoparticles. Of these various ligands, several binding motifs have been observed and classified. Depending on the chemistry of the ligand, different binding modes are classified as L, X, or Z-type ligands. In the case of L-type ligands, a neutral molecule donates a lone electron pair to a cationic nanoparticle surface atom. For an X-type ligand, a negatively charged molecule donates a single electron to a cationic nanoparticle surface atom forming a covalent bond. For Z-type ligands, a nanoparticle anchored metal donates two electrons to a neutral ligand.[26]

Despite the large body of literature on ligand exchange, very few reports have explored ligand exchange on more complex ternary, quaternary, and quinary materials such as $Cu(In_xGa_{1-x})(S_ySe_{1-y})_2$ or $Cu_2ZnSn(S_ySe_{1-y})_4$, with even less focusing on applications for photovoltaic devices. Due to the presence of many cationic species, the surface chemistry of these nanomaterials is less defined and subject to more variability, complicating ligand exchange pathways. Further complicating matters, the various cations can have significantly different reactivities as defined by Pearson hard-soft acid-base (HSAB) theory.[34] For example, in $CuInS_2$ (CIS) nanoparticles, indium is a hard acid while copper is a soft acid, thereby necessitating special consideration in pairing base ligands for ligand exchange. Multi-ligand, multi-step strategies have often been necessary due to the variety of surface sites on these ternary and quaternary chalcogenide nanomaterials.[36] Several reports have attempted to adapt ligand exchange methods for derivatives of CIGSSe and CZTSSe nanoparticles with varying degrees of success, with few making use of quantitative measures of native ligand removal. In a comprehensive study of alkylamine and thiol ligand binding on CIS, Diereck et al. explored ligand chemistry through proton nuclear magnetic resonance (^{1}H-NMR) studies, observing that L-type alkylamine ligands (OLA and octadecylamine) exhibit very tight binding, uncharacteristic of L-type ligands for other materials systems. This tight binding of alkylamine ligands generally necessitated temperatures greater than 100 °C for organic-organic ligand exchange facilitated by alkylamine desorption, further complicating ligand exchange pathways.[37] The lack of oleylamine desorption below 100°C and further difficulty of direct exchange with other species has been

observed in other reports, where molecular iodine was needed to facilitate exchange to other bulky carbonaceous ligands.[38] Other attempts in the literature using room temperature phase transfer exchanges with DAS have yielded poor removal of native OLA ligands (~50% removal) as determined by ^{1}H-NMR.[39]

In this report, various ligand exchange pathways were explored to yield exhaustive native ligand removal via a rapid process. Several criteria were identified for successful ligand exchange and subsequent utility of exchanged nanoparticles. First, the ligand exchange should remove the majority of native ligands to minimize carbonaceous residues. Second, the ligand exchange should not change the nanoparticle stoichiometry through etching of the nanoparticle surface, especially for low earth abundance elements such as indium. Third, the ligand exchanged nanoparticles should be dispersible at high mass concentrations exceeding 200 mg/mL for compatibility with scalable coating techniques such as blade coating and slot-die printing. Each of these criteria were systematically investigated and a sequential hybrid solvothermal organic and room temperature inorganic exchange was developed using pyridine and DAS. Native ligand removal of >98% was achieved and did not appreciably alter the stoichiometry of the as-synthesized nanoparticle. Finally, inks with mass concentrations exceeding 200 mg/mL were successfully prepared with colloidal stability on the order of months in low toxicity solvents such as DMSO. Blade coating and initial device fabrication was demonstrated with promising total-area power conversion efficiencies reaching 12.0%.

Experimental Section

Materials. Copper (I) Sulfide (99.99%), Ga (99.9999%), 1,2-ethanedithiol (98%), propylamine (99%), oleylamine (OLA, Technical grade, 70%), pyridine (anhydrous, 99.9%), acetonitrile (anhydrous, 99.9%), diammonium sulfide solution (DAS, 40-48 wt% aqueous solution), toluene (anhydrous, 99.8%), N-methyl formamide (NMF, 99%), dimethyl sulfoxide (DMSO, anhydrous, 99.9%), selenium pellets (99.995%), cadmium sulfate hydrate (99.996%), thiourea (>99%), dimethyl sulfoxide-D_6 (99.96 atom % D), 1,2-dichlorobenzene-D_4 (98 atom % D), chloroform-D (99.96 atom % D), toluene-D_8 (99.6 atom % D), ethylene carbonate (99.96%), copper (II) acetylacetonate (99.9%), indium (III) acetylacetonate (99.99%), gallium (III) acetylacetonate (99.99%), sulfur (99.99%), and hexanethiol (95%) were purchased from Sigma Aldrich and used as received with the exception of OLA, which was degassed through successive freeze pump thaw cycles, and gallium, from which surface oxide was removed with a blade. Indium (99.999%), hexanes (mixture of isomers, 99%), isopropyl alcohol (IPA, 99.9%), acetone (99.5%), and ammonium hydroxide (28.0-30.0% in H_2O) were purchased from Fisher Scientific and used as received. All chemicals were stored and dispensed under an inert nitrogen environment with < 0.1 ppm H_2O and O_2. Ultrapure water was produced using a Millipore Direct-Q 3 (18.2 MΩ at 25°C).

Synthesis of Cu(In,Ga)S_2 (CIGS) Nanoparticles. Nanoparticle synthesis was performed using a modified method from our previous report.[40] Briefly, separate Cu_2S and In/Ga precursor solutions were prepared. Propylamine and 1,2-ethanedithiol were added (2:1 mol:mol) to Cu_2S powder to form a 1.79 M (with respect to copper) solution, and to Ga and In (Ga/(In+Ga) ratio of 0.3) to form a 1.01 M solution. The Cu_2S solution was dissolved in a glovebox at room temperature overnight and the In/Ga solution was dissolved at 45°C on an argon purged Schleck line for several days. The transparent homogenous In/Ga solution was mixed with the transparent yellow/brown Cu_2S solution such that the Cu/(In+Ga) ratio was 0.92, yielding a homogenous transparent yellow/brown solution. This solution was transferred to a 100 mL reaction flask, diluted with 5.86 mL of OLA per mmol of In + Ga and connected to an argon purged Schlenk line. The solution was heated to 285°C over the course of approximately 30 minutes and allowed to dwell at reaction temperature for 90 minutes followed by natural cooling to room temperature, all with vigorous stirring. The reaction mixture was then precipitated with excess IPA and centrifugation. The supernatant was decanted and the nanoparticles were redispersed in hexanes at approximately 75 mg/mL followed by precipitation with IPA and centrifugation. The suspension and precipitation cycle was repeated two more times to remove all free OLA (as determined by ^{1}H-NMR, Figure S1). The final pellet was dried under argon flow and stored under an inert atmosphere for further use. Approximately 1 gram of CIGS nanoparticles were obtained from a single synthesis. For nanoparticle synthesis using metal acetylacetonate salts and sulfur in OLA, previous literature methods were used.[16,19]

Ligand Exchange. Pyridine ligand exchanges were performed by first dispersing the dry CIGS nanoparticles in toluene at 100 mg/mL using sonication. The dispersed nanoparticle ink was transferred into a borosilicate glass microwave reaction vial with a polytetrafluoroethylene (PTFE) coated magnetic stir bar and diluted with pyridine at a 9:1 pyridine:toluene vol:vol ratio. The microwave reaction vial was crimp sealed with an aluminum cap over a PTFE coated silicone septa. The microwave vial was heated using a Biotage Initiator EXP 400W microwave reactor, equipped with an in-situ IR temperature sensor and pressure gauge. The microwave vial was heated to 150°C for 30 minutes with magnetic stirring, followed by natural cooling to room temperature. The nanoparticles were then precipitated using

excess hexanes and centrifugation. The supernatant was decanted. If additional pyridine cycles were performed, the pellet was redispersed in pyridine and again transferred to a microwave vial. The aforementioned procedure was repeated up to three times for successive pyridine cycles.

The final pyridine exchanged CIGS pellet was then dispersed in 10:1 vol:vol NMF:DAS at approximately 20 mg/mL through vortex mixing in a fluorinated ethylene propylene (FEP) vessel (significant particle adsorption to glass vessel walls was observed, thus the use of a polymer vessel enabled increased yields). An immiscible phase of hexanes of equal volume was added. The mixture was allowed to stir at room temperature for 90 minutes, after which, the polar NMF/DAS phase was removed and added to a clean vial. The liquid-liquid interface between the polar and non-polar phase was intentionally rejected to prevent collection of poorly exchanged particles which typically aggregated at the liquid-liquid interface. An equal volume of hexanes was again added to the mixture. The two-phase mixture was stirred for an additional 30 minutes to allow any residual native ligand in the polar phase to segregate to the hexanes. The polar phase was removed, rejecting the liquid-liquid interface, and transferred to a centrifuge tube. The nanoparticles were precipitated with excess acetone and centrifugation. The supernatant was decanted and the pellet was redispersed in acetonitrile at approximately 15 mg/mL and precipitated with acetone. The decanting, suspension in acetonitrile, and precipitation with acetone and centrifugation was repeated one additional time. The supernatant was decanted and the nanoparticles were dried under a nitrogen flow for 30 minutes. The dry particles were stored under nitrogen for further use.

Single step exchanges were performed by first dispersing the native ligand capped CIGS nanoparticles in hexanes at 20 mg/mL using sonication. Then, a 10:1 vol:vol mixture of NMF and DAS solution were added as an immiscible polar phase. The mixture was stirred for 16 hours, during which time CIGS nanoparticles migrated from the upper hexanes phase to the lower NMF/DAS phase. The polar phase was removed while rejecting the liquid-liquid interface and transferred to a fresh vial. An equal volume phase of hexanes was added and allowed to stir for 30 minutes. Finally, the polar phase was removed, rejecting the liquid-liquid interface, and washing was performed as described for the hybrid ligand exchange.

Nanoparticle Ink Preparation and Coating. The dry ligand-exchanged nanoparticles (from single step or hybrid ligand exchanges) were weighed and dispersed in DMSO at concentrations ranging from 150-250 mg/mL, typically at 225 mg/mL using sonication. The resulting viscous ink was then blade coated on soda lime glass or molybdenum coated soda lime glass substrates using a multipass auto-blade coater constructed from a modified 3D printer (KClone K200). First, the blade coater stage and substrate were heated to 80°C and 12 µL of ink were dispensed on the edge of a 2"x1" substrate. A 100 µm blade gap and blade speed of 25 mm/s was used, with two passes down and up the substrate using a borosilicate glass rod as a blade. The film was allowed to dry for four minutes at 80°C. The film was then annealed at 300-400°C for 60-90 s in an inert atmosphere followed by 30 s of natural cooling on aluminum foil rails, and finally quenching on a room temperature aluminum block. At 225 mg/mL, each coating typically yielded a 300 nm thick layer. Successive coatings could be repeated for desired thickness. For preparing the conventionally prepared nanoparticle thin films, dry particles were dispersed in hexanethiol at 250 mg/mL. Coatings were performed and annealed in air as described in previous literature.[16,18,19]

Device Fabrication. Molybdenum was DC magnetron sputtered on soda lime glass substrates with a final thickness of 800 nm. Nanoparticle inks were coated with four layers as described previously. Following coating, 10 nm of NaF was evaporated onto the CIGS nanoparticle films using E-beam evaporation. The CIGS films were then selenized in a graphite box in a tubular furnace under an argon atmosphere with selenium pellets at 500-550°C for 10-20 minutes. After selenization, CdS (50 nm) was deposited by chemical bath deposition. Then, i-ZnO (80 nm) and ITO (220 nm) were deposited by RF sputtering. Finally, Ni/Al (100 nm/1.5 µm) grids and a MgF_2 (100 nm) antireflection coating were deposited by E-beam evaporation. Devices were isolated with mechanical scribing with a device total-area of approximately 0.47 cm^2 (exact areas determined by image analysis, Table S3) and a grid shading of 4%.

Characterization. Capillary gas chromatography mass spectrometry (GC-MS) analysis was performed with an Agilent 5975C mass spectrometer with an electron energy of 70 eV, ion source temperature of 250°C, and 30-meter DB-5 capillary column (250µm i.d. X 0.25µm film thickness). OLA was diluted in dichloromethane for GC-MS measurements. X-ray diffractograms (XRD) were collected on a Rigaku Smart Lab diffractometer with a Cu Kα (λ = 1.5406 Å) source operated at 40 kV/44 mA in in parallel beam (PB) mode at an angle of 0.5 degrees. Raman spectra were collected using a Horiba/Jobin-Yvon HR800 Raman spectrometer with a 632.8 nm excitation laser wavelength. Quantitative elemental composition measurements were taken on a Fisher XAN 250 X-ray Fluorescence (XRF) instrument at 50 kV voltage with a silicon drift detector, primary nickel filter, and flowing helium gas purge. ^{1}H-NMR spectra were collected with a Bruker AV-III-400-HD using a relaxation time of 6 seconds and 32 scans. Heat up ^{1}H-

NMR was performed on a Bruker DRX500-2 NMR with a relaxation time of 6 seconds and 8 scans. DMSO-D_6, 1,2-dichlorobenze-D_4, and toluene-D_6, and chloroform-D were used as deuterated solvents and quantitation was performed using ethylene carbonate as an internal standard. During *in-situ* heat up experiments, 1,2-dichlorbenzene-D_4 was used as a solvent in a screw cap NMR tube, and the sample was allowed to equilibrate for approximately five minutes at each temperature prior to measurement. FTIR spectra were collected with a Thermo-Nicolet Nexus 670 FTIR in transmission mode using either NaCl crystal or soda lime glass as substrates. Thermogravimetric Analysis (TGA) was performed using a TA Instruments Q50 with an alumina pan and platinum holder at a heating rate of 10°C/min under an argon atmosphere. Scanning Electron Microscopy (SEM) images were taken using a FEI Quanta 3D FEG Dual-beam SEM with an Everhart-Thornley Detector at an accelerating voltage of 10kV and working distance of 10 mm. Profilometry was performed using a Dektak 6M stylus profilometer with a 12.5 μm diameter diamond tip stylus. Thickness measurements were taken using mechanically scribed trenches. X-ray Photoelectron Spectroscopy (XPS) was performed on a Kratos AXIS ULTRA DLD Imaging XPS with monochromatic Al Kα radiation (1486.6 eV). Peak fitting was performed on CasaXPS using Voigt peak profiles and linear backgrounds. The peak position of C 1s was set to 285 eV and for the S 2p photoelectron transition the doublet separation between S $2p_{1/2}$ and $2p_{3/2}$ was set at 1.20 eV. Capacitance-voltage measurements were collected using a Hewlett Packard 4284A LCR meter operated at 100 kHz. Transmission electron microscopy (TEM) images and scanning tunneling electron microscopy energy dispersive x-ray spectroscopy (STEM-EDS) measurements were taken on a Talos 200X TEM with four silicon drift detectors with lacey carbon grids for imaging and molybdenum grids for STEM-EDS. A FEI Helios 600 Dualbeam FIB with a gallium ion beam was used to prepare the FIB samples.

Results and Discussion

A wide variety of synthetic methods have been developed for CIS and CIGS nanoparticles.[23] In this report we adapted a synthetic pathway from our previous work that makes use of high purity elemental indium (99.999%), gallium (99.99999%), and copper (I) sulfide (99.99%) as precursors in amine-thiol solutions.[40] A gram-scale one-pot heat up reaction was employed using OLA as a reaction solvent/ligand as described in the experimental section. The advantage of this synthetic pathway is that it eliminates potential anionic impurities present in commonly used metal salts such as halides, nitrates, sulfates, acetate, acetylacetonates, etc.[22,23] It is well known that anions from conventional metal salts can bind to nanomaterial surfaces and alter their growth and/or subsequent optoelectronic properties,[26] or in the case of oxygen containing anions, introduce high resistivity oxide secondary phases.[22,41] Using only Cu_2S, In, and Ga prevents the introduction of non-sulfide, contaminating anionic X-type ligands typically present in metal salts. XRF measurements of as synthesized nanoparticles typically revealed elemental ratios of 0.92 for Cu/(In+Ga) and 0.29-0.30 for Ga/(In+Ga). The particles were imaged as shown in Figure S2 and have an average size of approximately 10 nm.

OLA has been widely employed as a solvent/ligand for the synthesis of CIS and CIGS nanoparticles due to the high colloidal stability it affords. OLA also exhibits favorable binding on indium (III) and gallium (III) surface sites due to favorable HSAB interactions.[22,23] However, OLA is almost always used as a technical grade mixture, a mixture of primary amines and other trace alkyl components. After degassing by successive freeze pump thaw cycles under vacuum (which removes more volatile components of the mixture), the technical grade OLA was run through GC-MS to identify the components of the degassed technical grade mixture. An understanding of this mixture is important for the design and characterization of adequate ligand exchange pathways. Table S1 details the compositional makeup of the technical grade OLA. Of the degassed mixture species, 87.3% contained a carbon-carbon double bond, either as OLA or hexadeceneylamine. Additionally, no X-type impurities were observed as is reported by others.[37] Using ^{1}H-NMR, the protons of the alkene region are distinctly separate from the alkyl chain and amine protons. As such, this provides a convenient means of quantifying the OLA molecules bound to the nanoparticle surface. Figure 1 a) shows the ^{1}H-NMR of OLA, as well as OLA capped CIGS nanoparticles. Distinct peak broadening and disappearance of the amine protons and CH_2 protons closest to the amine are observed which are all characteristic of surface bound OLA. The peak broadening is caused by immobilization of the ligand molecule at the nanoparticle surface and becomes more pronounced the closer the protons are to the bound polar head group. In the case of the amine and neighboring alkyl chain protons, the peak broadens so significantly that it becomes indistinguishable from the noise.[37] The amine is able to donate its lone pair electrons on the nitrogen atom to cationic metals on the nanoparticle surface. Typically, this binding is described as a weakly bound adsorption like process, and amines can be desorbed as simply as through dilution. This "weak" binding has been observed for binary metal chalcogenides such as CdTe and PbSe.[42] Interestingly, OLA and octadecylamine (ODA) have been shown to exhibit exceptionally tight binding to CIS nanoparticles in previous work by Diereck et al.[37] Conventional spontaneous desorption was not observed for OLA and ODA ligands at room temperature. Desorption was only observed when the CIS nanoparticles were exposed to temperatures in excess of 110°C.[37] Due to differences in synthetic pathway and the inclusion of gallium (a harder acid than indium), we

repeated their temperature dependent ^{1}H-NMR OLA binding study on CIGS nanoparticles synthesized via the amine-thiol precursor route.

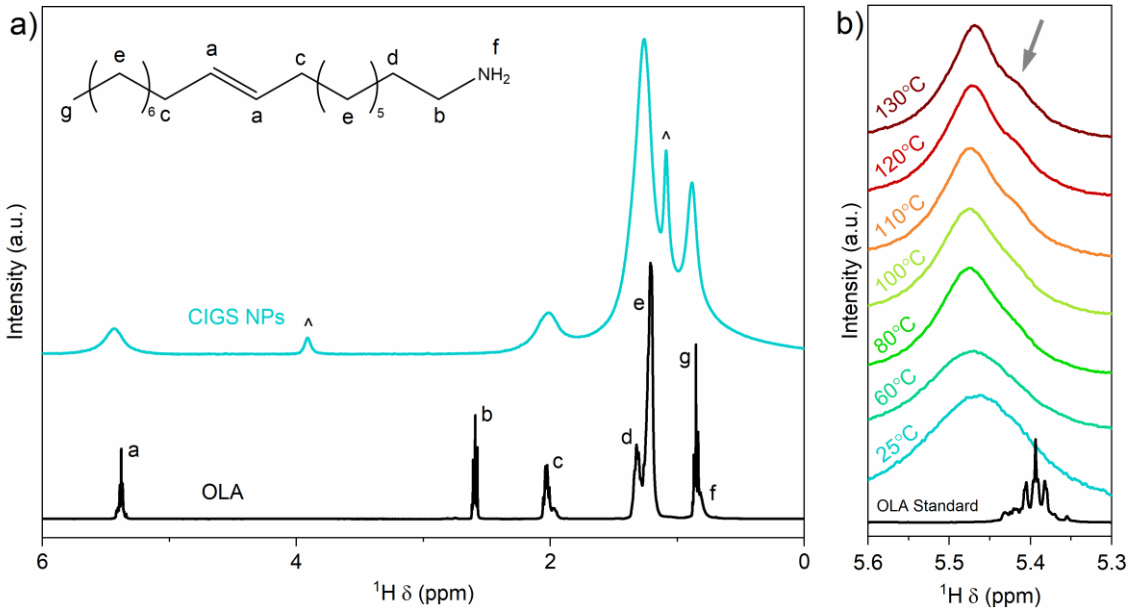

Figure 1. a) *^{1}H-NMR of OLA capped CIGS NPs as compared to neat OLA (^ denotes residual IPA from particle washing) and* ***b)*** *In-situ heat-up ^{1}H-NMR of OLA capped CIGS NPs from 25°C to 130°C as compared to neat OLA. Chloroform-D and 1,2-dichlorobenzene-D_4 were used as deuterated solvents in a) and b) respectively*

As shown in Figure 1 b), a shoulder peak emerges at 5.44 ppm, onset at approximately 110°C. This shoulder is attributed to dynamically absorbed/desorbed OLA, confirming similar results to what was observed by Diereck et al.[37] As a result, elevated temperature in the solution phase is needed to induce OLA desorption. Furthermore, the removal of OLA from a thin film was probed using FTIR. CIGS nanoparticles were dropcast from chloroform onto NaCl crystals and spectra were recorded at the same location (and thereby same pathlength) on the CIGS thin film before and after annealing at 300°C for 5 minutes in a nitrogen atmosphere. As shown in Figure 2, no appreciable change in the intensity of C-H stretches around 2924 cm^{-1} was observed, demonstrating the low volatility of OLA ligands in a thin film. Use of higher temperature annealing risks the decomposition of OLA into graphitic carbon under an inert atmosphere. While air annealing can prevent the formation of graphitic carbon through the combustion of the organic species, it risks the oxidation of the nanoparticle precursor film.[20] Oxide containing precursor films generally require an additional reduction step,[43] otherwise residual oxide content can be observed in the final selenized film,[44] and could substantially increase series resistance.

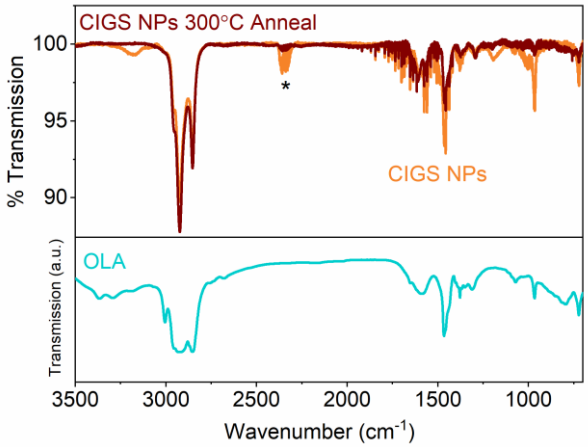

Figure 2. *FTIR of neat OLA, and comparison of OLA capped CIGS NPs with OLA capped CIGS NPs annealed at 300°C for 5 minutes under nitrogen atmosphere (* donates atmospheric CO_2).*

To remove the carbonaceous impurities stemming from native OLA ligands, a variety of ligand exchange pathways were investigated. Both volatile organic ligands and inorganic sulfide ligands were analyzed with respect to their ability to remove OLA, preserve nanoparticle stoichiometry, and retain colloidal stability at high mass concentrations. Pyridine was investigated as a target volatile organic species due to its weak basicity, relatively low boiling point, and previous success in ligand exchange for photovoltaics literature.[29] Similar to alkylamines, pyridine can bind to cationic surface atoms as an L-type ligand through its nitrogen lone pair electrons, thus native ligand desorption followed by pyridine adsorption was the targeted exchange mechanism, driven by a molar excess of pyridine. Traditionally, ligand exchanges with pyridine are performed at reflux conditions. However, due to the temperature-dependent nature of OLA desorption, pyridine's boiling point of 115°C barely enters OLA's thermal desorption regime as observed in heat up ^{1}H-NMR. As such, a microwave-assisted solvothermal approach was investigated as a means to bypass atmospheric pressure boiling point limits, while microwave radiation could selectively excite the polar head groups of the ligands to aid in exchange. Use of a sealed vessel allowed pressurized reaction conditions above the boiling point of pyridine, and farther into the desorption regime of oleylamine. A temperature and time of 150°C for 30 minutes was selected to facilitate ligand exchange, a temperature well above the OLA desorption onset. Due to pyridine's near universal miscibility, ligand exchange was performed in a single liquid phase. While OLA capped nanoparticles were readily dispersible in non-polar media such as hexanes, toluene, and chloroform, neat pyridine was observed to induce significant flocculation due to its relatively higher polarity (ε = 12.4). To bypass this, the particles were first suspended in toluene followed by dilution with pyridine (1:9 vol:vol toluene:pyridine) to allow for proper dispersion. To the best of our knowledge, this is the first report of microwave-assisted solvothermal ligand exchange reaction.

After the heating cycle and cooling of the dispersion back to room temperature, the pyridine exchanged particles would remain dispersed directly after exchange with the onset of settling observed after an hour with no agitation. The nanoparticles were precipitated with excess hexanes and centrifugation. Prior to the exchange, hexanes were a suitable solvent to disperse the nanoparticles, a qualitative indication of OLA removal by their action as an antisolvent post-exchange. However, after precipitation, the particles did not fully redisperse in additional pyridine, with many visible aggregates in solution. The significant decrease in observed colloidal stability is attributed to the significantly less bulky tail group of pyridine's ring, thereby providing less steric repulsion between adjacent nanoparticles and allowing for some degree of aggregation. To further probe pyridine's ability to remove OLA ligands, successive pyridine exchange cycles were performed to assess the upper limit of its OLA removal ability. Due to the compromised colloidal stability and rapid settling, quantitative measurements of residual OLA in colloidal dispersions using ^{1}H-NMR were not feasible. In its place, TGA was used to probe the OLA removal capacity of pyridine as shown in Figure 3. Each of the pyridine exchanged nanoparticles were dried under vacuum prior to TGA. Note that TGA measurements were run under inert atmosphere to prevent particle oxidation (and thereby changing the mass of the CIGS nanoparticles), thus the mass loss at higher temperatures may not be fully representative of the total mass of OLA due to coke formation from incomplete pyrolysis of OLA.[20] Mass loss up to 500°C is shown in Figure 3, which is the maximum processing temperature used for later device fabrication.

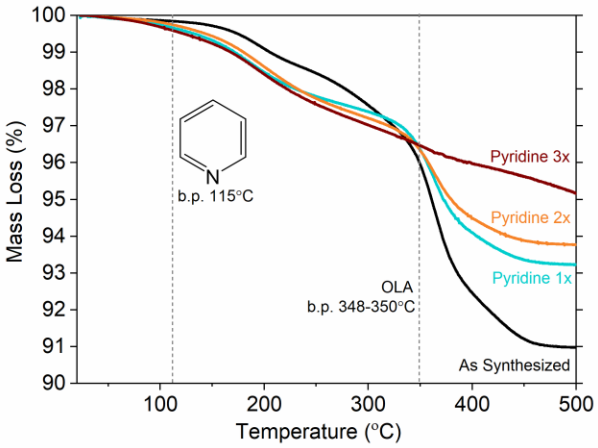

Figure 3. *TGA of CIGS nanoparticles with as synthesized OLA ligands as compared to CIGS nanoparticle ligand exchanged with pyridine in 1, 2, and 3 successive cycles.*

As shown in Figure 3, pyridine was able to begin OLA removal after a single cycle. However, even after up to three successive pyridine exchanges, a significant portion of OLA as denoted by the mass loss event around 350°C remains. This suggests that there is a critical amount of OLA that can be removed by pyridine-based ligand exchanges, implying there may be an equilibrium of pyridine/OLA capping as defined by their relative strength as ligands. Further, while pyridine is an intermediate base as defined by HSAB theory, there may be some preference to specific metal surface sites, leaving native ligands on other surface sites bound. Interestingly, after three pyridine exchanges, the TGA mass loss was significantly more linear, not showing a discrete mass loss event at the boiling point of OLA. However, due to the lack of any discrete mass loss events in the three-pyridine exchange case, it is unclear if the observed mass losses are the result of solely pyridine evaporation, decomposition of the nanoparticle, and/or simply from atmospheric or cleaning procedure induced adsorbates on the alumina TGA pan decomposing during heat up. Future work aims to further clarify the TGA data for the three pyridine exchange case. Further ink formulation of pyridine exchanged nanoparticles was marred by the poor colloidal stability and rapid settling of pyridine capped particles, thereby not meeting the need for high mass concentration inks suitable for blade and slot die printing methods. As such, pyridine exchanges alone were deemed to be a largely ineffective means of complete native ligand removal.

As a means to bypass the limitations of organic ligands such as pyridine, ligand exchange with inorganic sulfide ligands was investigated as an alternative. In the case of OLA to sulfide ligand exchange, sulfide anions bind to the cationic sites on the nanoparticle surface. To maintain charge neutrality, when the neutral L-type OLA ligand is displaced by an anionic sulfide ligand, counter cations of the sulfide salt must be retained to form a net charge neutral nanoparticle. If any X-type ligands are present on the nanoparticle surface (such as 1,2-ethanedithiol, which is a part of the reaction mixture during synthesis), a metathesis type ligand exchange is possible. In this exchange, the cation from the sulfide salt coordinates with a thiolate and induces desorption. The sulfide would then covalently bind to metal cations on the nanoparticle surface as an X-type ligand.[26] Of sulfide salts, sodium and DAS are the two most readily available. However, due to the possible retention of cationic species, sodium sulfide was avoided to prevent an excess of sodium from being retained in the film. While sodium is a favorable dopant species in CIGSSe photovoltaics, too much can harm optoelectronic properties.[45] Therefore, we opted to control sodium content post film deposition for more fine control and selected DAS as the ligand of choice. In the case of DAS, charged ammonium cations can be volatilized as ammonia gas, leaving just protons as a charge balancing cations. Further, during annealing or selenization, the DAS ligand could simply volatilize as ammonia and hydrogen sulfide gas.[46]

A two-phase ligand exchange was employed as is common in the literature.[35] First the nanoparticles were dispersed in non-polar hexanes. Then an immiscible polar phase of NMF and aqueous DAS solution was added. With stirring, a gradual phase transfer of the nanoparticles in the upper non-polar phase to the polar phase was observed over the course of 16 hours. After purification and drying as described in the experimental section, the nanoparticles could be redispersed in deuterated DMSO forming colloids that did not settle for months. As such, ^{1}H-NMR quantitation of OLA removal was possible. Using ethylene carbonate as an internal standard, remaining OLA was quantified using peak fitting and integration of the alkene proton peak, which is distinctly separate from the chemical shift of other trace species such as washing solvents. As shown in Figure 4 a), the sulfide exchange was observed to be extremely effective at removing OLA, removing 97.3% of the native ligands, determined through comparison of the as-synthesized and ligand exchanged alkene peak integration. This result is a substantial improvement on previous quantitative reports in the literature, whereby only ~50% of OLA was removed with DAS. In the previous literature report, pre-exchanged particles were observed to have a sharp peak at 5.35 ppm, slightly offset from the broadened bound alkene peak at approximately 5.4 ppm.[39] This sharp peak, likely being free OLA, may have inhibited their sulfide exchange by altering the equilibrium, highlighting the need for sufficient nanoparticle purification post-synthesis to remove free OLA. In this work, sufficient nanoparticle washing was determined through ^{1}H-NMR, where no free OLA resonance was observed after four successive precipitation/resuspension cycles with isopropyl alcohol and hexanes as antisolvent and solvent respectively as shown in Figure S1. Additionally, we believe the longer duration of the sulfide exchange used in this report allowed for more complete exchange. However, this longer duration exchange also exposes the nanoparticles to the fairly aggressive DAS species for a longer time, raising concerns of nanoparticle surface etching. XRF measurements of DAS exchanged nanoparticles revealed that some copper was in fact etched from the nanoparticle during the exchange. DAS is known to dissolve certain metal chalcogenides such as copper selenide, so selective etching of copper from the chalcogenide nanoparticle is not unexpected and has been observed in previous reports.[47]

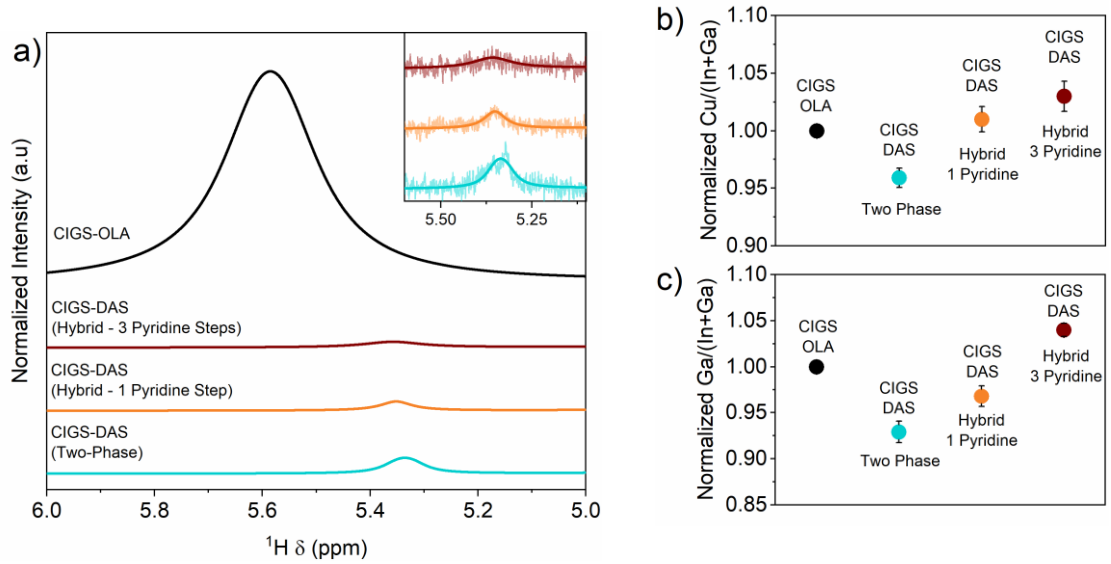

Figure 4. a) *Fitted ^{1}H-NMR comparing alkene proton resonance on OLA capped CIGS nanoparticles and hybrid pyridine/DAS exchange and DAS exchange (inset shows fitted data superimposed on experimental data for each of the CIGS-DAS exchanges). The shift in the alkene peak positions between the CIGS-OLA spectrum and CIGS-DAS spectra are due to the use of different deuterated solvents, where Toluene-D_8 and DMSO-D_6 were used, respectively.* ***b)*** *Cu/(In+Ga) and* ***c)*** *Ga/(In+Ga) ratios normalized to 1 for the respective exchange methods measured by XRF (As synthesized CIG = 0.92 and GIG = 0.29).*

Additionally, a corresponding drop in Ga/(In+Ga) ratio was observed, implying that Ga may also be selectively etched. While this copper and gallium etching could be compensated for by increasing the relative metal content of the original nanoparticle, one of the goals of solution processing is to increase materials utilization. Thus, it is advantageous to avoid this etching outright.

It was hypothesized that the combination of the solvothermal pyridine exchange followed by the DAS exchange would allow for significantly reduced residence time in the DAS containing polar phase, thereby decreasing etching of metals while also substantially decreasing the total time required for the ligand exchange. The pyridine exchange is able to remove a portion of OLA, providing holes in the protective layer of sterically hindering and hydrophobic alkyl chains, allowing DAS to access the nanoparticle surface more readily. This sequential exchange was performed as described in the experimental section, where the pyridine-exchanged particles were directly dispersed in the NMF/DAS phase and allowed to stir for a total of 120 minutes, and is referred to as the hybrid ligand exchange (hybrid LigEx). The resulting exchanged particles were purified and dried, followed by analysis by quantitative ^{1}H-NMR and XRF. The two-step hybrid organic-inorganic exchange was able to surpass the OLA removal attained by the single step two-phase method. No traces of pyridine were observed in the ^{1}H-NMR spectra, demonstrating its ease of displacement by DAS as shown in Figure S4. Additionally, XRF confirmed negligible copper etching and substantially decreased gallium etching, confirming the hypothesis that decrease in DAS containing polar phase residence time can prevent metal etching. The removal of OLA could be further driven to completion by repeating the pyridine exchange several times. ^{1}H-NMR quantitation of hybrid exchanged nanoparticles with three pyridine exchanges show near complete removal of the alkene peak. For the hybrid LigEx with 1 pyridine cycle, 98.4% of the original alkene intensity was removed. For the hybrid LigEx with three pyridine cycles, quantitation was also performed yielding 98.4% removal again, however, we note that the very low signal to noises ratio at that level of OLA removal likely yields inaccurate quantitation for this sample. To confirm the hybrid LigEx did not alter crystalline phase or induce the formation of any amorphous phase material, XRD and Raman were run on nanoparticles exchanged with both the one-step, two-phase transfer method and hybrid LigEx as is shown in Figure S5. No changes in crystalline phases or evolution of secondary phase formation were observed via both XRD and Raman.

With near exhaustive OLA removal obtained by the rapid hybrid exchange method, ink formulation was explored with the goal to form stable inks with mass concentrations exceeding 200 mg/mL. As previously mentioned, these high mass concentration inks allow us to bypass non-scalable and low materials utilization coating techniques such as spin coating and enables scalable coating techniques such as blade coating. Various polar aprotic solvents were

tested such as acetonitrile, DMF, NMF, formamide, and DMSO. Polar protic species such as alcohols and water (which were observed to disperse the ligand exchange nanoparticles well) were avoided due to their ability to bind as alkoxide and hydroxide ligands, which are known to decompose to metal oxides.[48] While all tested polar solvents could disperse the sulfide ligand exchanged nanoparticles to some extent, formamide, NMF, and DMSO were able to disperse the exchanged nanoparticles at mass concentrations exceeding 200 mg/mL without aggregates. Formamide has been previously investigated as a solvent for DAS exchanged $CuInS_2$ nanoparticles. However, in work by Dierick et al., it was observed that the use of formamide as a solvent was responsible for the oxidation of dropcast nanoparticle CIS thin films upon annealing in an inert atmosphere. They observed this oxidation in XPS via a transition of surface S^{2-} to positive oxidation state sulfur bonded to oxygen as SO_2, SO_3-, and/or SO_4^{2-} moieties. Furthermore, they observed that the surface oxidation inhibited sintering of the sulfide capped nanoparticles.[46] As such, we chose to avoid formamide and its derivatives, NMF and DMF, for ink formulation. Ideally, a solvent molecule that does not contain oxygen could completely avoid oxidation concerns. Acetonitrile is such a solvent, however, acetonitrile-based inks were only able to disperse a portion of the ligand exchanged nanoparticles and thereby contained a substantial amount of aggregates. DMSO was observed to disperse the sulfide-capped nanoparticles with ease, and formed stable inks at mass concentrations of up to 250 mg/mL without gelling. These inks were stable for over two months when stored in an inert atmosphere without settling and for several days when stored in air. However, as an oxygen containing molecule, oxidation of the nanoparticle films similar to what had been observed with formamide was a concern. To test if DMSO based inks could induce particle oxidation, XPS was performed on two dropcast thin films, one containing DMSO and sulfide exchanged CIGS, and a control of sulfide exchanged CIGS in the non-oxygen-containing solvent, acetonitrile. Both films were coated and annealed at 300°C for 90s in a nitrogen filled glovebox. As shown in Figure 5 a) through d), both films appeared identical under XPS and neither contained the Sulfur IV oxidation state peak observed at 169.5 eV in Dierick et al.'s previous report that made use of formamide as a solvent.[46] Furthermore, analysis of gallium, which forms the most stable oxide of the cations in CIGS did not show any discernable oxide content, only exhibiting a single gallium peak as is commonly observed for CIGS/CIGSSe.[49] This lack of oxidation and the high stability of DMSO based inks coupled with its low toxicity made for an attractive ink for device fabrication.

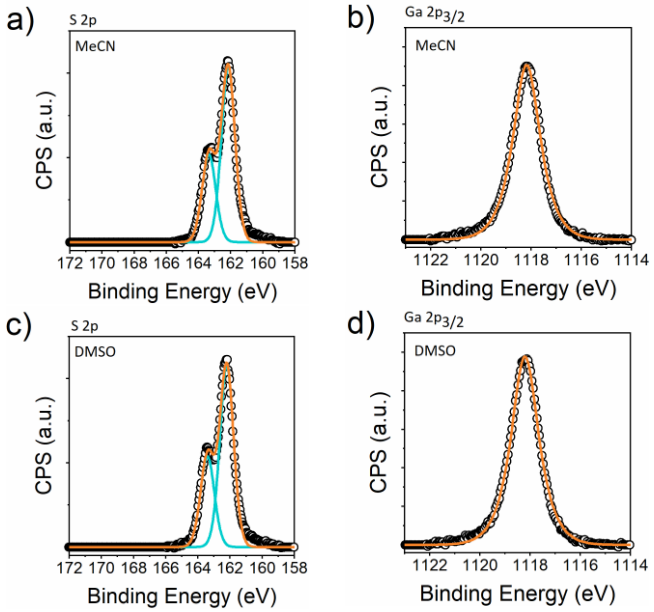

Figure 5. a) *and* ***c)*** *XPS of sulfur 2p peak showing absence of any sulfoxide (169.5 eV) and* ***b)*** *and* ***d)*** *XPS of gallium $2p_{3/2}$ peak showing absence of any gallium oxide species for both the control acetonitrile and DMSO inks demonstrating absence of solvent induced oxidation. Circles, blue lines, and orange lines denote experimental data points, individual peak fits, and overall fit, respectively.*

Blade coating was selected as a scalable coating method for ligand exchanged inks and was performed using a custom built automated blade coater based on a KClone K200 3D printer with controllable substrate-blade gap, coating speed, coating pattern, and substrate temperature. DMSO was observed to dewet from the edges of both soda-lime glass and molybdenum coated soda lime glass substrates during long drying periods at room temperature. A heated bed was found to be effective in enabling rapid drying prior to edge dewetting. A bed temperature of 80°C was found

to be most effective. Using the conditions described in the experimental section, highly uniform coatings at thicknesses of approximately 300 nm per coating were obtained. Sequential coatings could be performed by annealing the films at a minimum of 300°C for 90 s between coatings. If not sufficiently annealed between coatings, it was observed that subsequent coatings would redisperse underlying layers and yield rough and discontinuous films. After four successive coatings, remarkably smooth films with an average and RMS roughness of 5.07 and 6.25 nm, respectively, were obtained at thicknesses of approximately 1200 nm as shown in the SEM cross section in Figure 6 a). Additionally, the films were free of any microcracks as evidenced by SEM plan view as shown in Figure 6 b). A larger area optical micrograph and profilometry scan are shown in Figure S6, further demonstrating the high quality of the coated films. The hybrid LigEx films were uniquely resistant to microcracking, which has been a significant concern and the topic of entire research articles in other nanoparticle based coating methods. In these reports, additional carbonaceous long chain surfactants, DDT or OLA, were incorporated in the ink through either reduced nanoparticle washing, or direct addition, counterproductive to the goal of removing carbon contamination.[50,51]

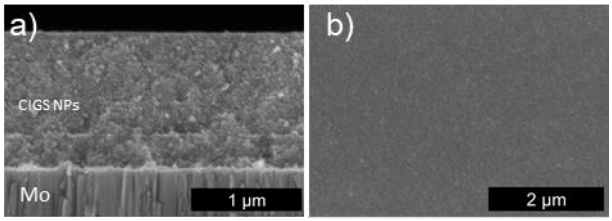

Figure 6. a) *SEM Cross-section and* ***b)*** *plan view of hybrid ligand exchange nanoparticle film coated by blade coating*

Selenization of coated nanoparticle films was performed using a tubular furnace with ~300 mg of elemental selenium pellets under an argon atmosphere at 500°C. XRD and Raman analysis of the selenized films reveal conversion of the original CIGS nanoparticles to sulfur depleted CIGSSe with improved crystallinity. Conversion from sulfide to selenide is clearly visible in the shift in XRD peaks, as well as reduction in intensity of the sulfide CIGS A1 Raman peak, centered at approximately 300 cm^{-1}, and the emergence of a sharp A1 Raman peak of selenide $Cu(In,Ga)Se_2$ at approximately 178 cm^{-1}. Additionally, no secondary phases were found, notably residual elemental selenium or $Cu_{2-x}Se$ as shown in Figure 7 (however, it should be noted that Raman spectroscopy is surface sensitive, thus may not be representative of the back of the absorber layer). As such, no pre or post selenization treatment in highly toxic potassium cyanide were needed, reducing the toxicity and number of steps in film processing. XRF measurements showed post-selenization elemental ratios of 0.92 for Cu/(In+Ga) and 0.28 for Ga/(In+Ga).

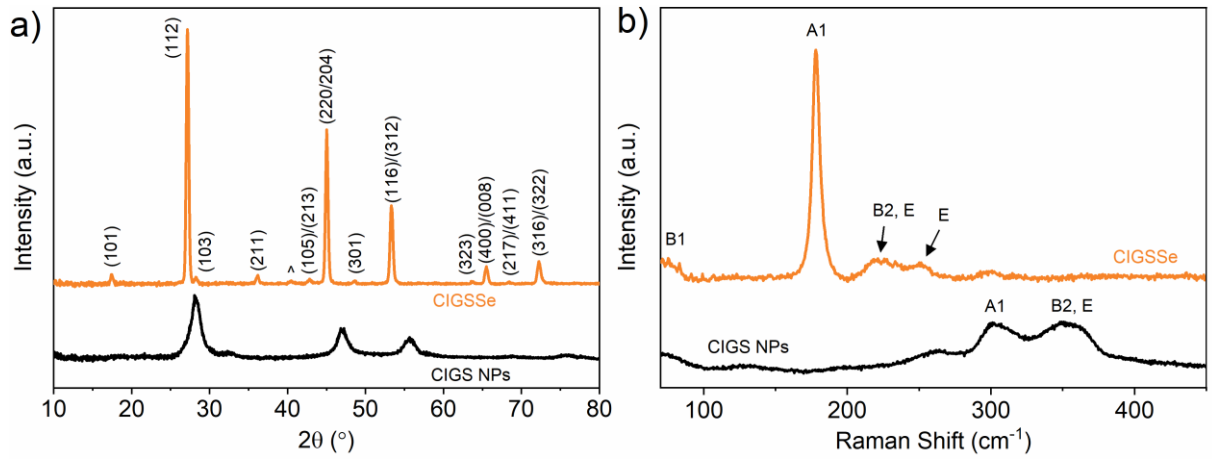

Figure 7. a) *XRD and* ***b)*** *Raman of CIGS nanoparticles and selenized CIGSSe from hybrid ligand exchanged ink (^ denotes the molybdenum substrate's XRD peak).*

Further analysis of the carbon content was performed on the coated and selenized films using FTIR and Raman spectroscopy. A thickness normalized (profilometry calibrated) comparison of an annealed unexchanged nanoparticle

film, annealed ligand exchanged nanoparticle film coated from DMSO, and selenization of the ligand exchanged nanoparticle film was performed using FTIR on soda lime glass substrates. As shown in Figure 8, a significant reduction in C-H stretch intensity is observed when comparing unexchanged nanoparticle films with ligand exchanged nanoparticle films.

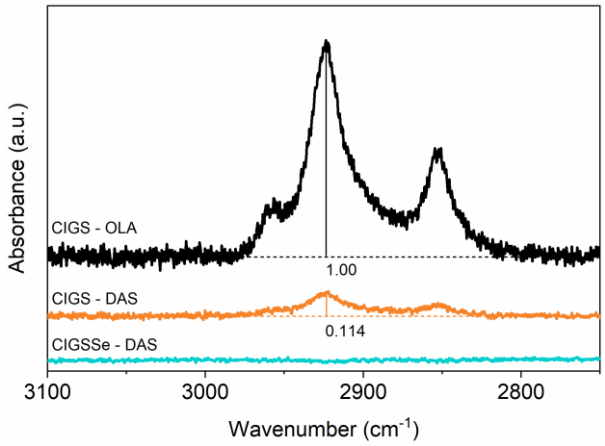

Figure 8. *Thickness normalized FTIR on blade coated nanoparticles films of CIGS – OLA (coated from hexanethiol), Hybrid CIGS – DAS (coated from DMSO), and selenized hybrid CIGS – DAS (CIGSSe, 500°C, 10 min) on sodalime glass.*

After selenization, there is a complete absence of C-H stretches. If all C-H intensity is attributed to residual OLA, there is a small discrepancy between the quantitative ^{1}H-NMR and the FTIR of the coated CIGS – DAS film. It is believed this discrepancy is due to the entrainment of coating solvent in the annealed nanoparticle film, which has been observed in other solution processed literature.[52] While selenized films of ligand exchanged CIGS nanoparticle films were free of C-H stretch in FTIR, Raman spectroscopy was used to probe graphitic carbon-carbon bonds. Due to Raman's low penetration depth of only a few hundred nanometers, a thin ~300 nm thick film was used. Miniscule, but discernable peaks were observed in Raman corresponding to graphitic carbon-carbon bonds as shown in Figure S7. We believe this residual signal is from the remaining ~1% of initial OLA, and potentially some of the entrained solvent decomposing during selenization.

Selenization of hybrid exchanged CIGS nanoparticles on molybdenum substrates for device fabrication was performed and compared with selenized CIGS nanoparticle films from conventional methods (OLA ligands, acetylacetonate salts for synthesis, hexanethiol as a coating solvent, coating and annealing in air). Sodium for both films was provided using 10 nm of electron beam evaporated sodium fluoride and both were selenized at 500°C for 20 minutes. Since potassium cyanide was not needed for the hybrid LigEx films to correct elemental ratios, remove surface oxide or $Cu_{2-x}Se$ secondary phases, potassium cyanide was also not used in the conventional device as has been used prior to selenization in our group's previous reports.[16,18] This allowed for direct comparison between the two devices, decoupling any effects that residual potassium could have on the electronic or morphological properties. A marked difference is immediately observed between the selenized conventional and hybrid LigEx films, with a large unsintered layer/carbon residue layer observed for the unexchanged nanoparticles. As has been observed consistently in solution processed CIGS literature, presence of significant carbon can inhibit grain growth and limit the ultimate thickness of large grains while leaving a discrete carbon residue layer. For hybrid ligand exchanged films, grains appear to span the thickness of the film, however a thin nanocrystalline layer is still sometimes observed at the back contact. This layer was further probed using STEM-EDS to elucidate the species present as shown in Figure S8. For the conventional method, the resulting fine grain layer after selenization had a composition of C/(Cu+Se) of 0.88, and as seen in Figure 9a, generally had a thickness of ~600 nm. When a fine grain layer was observed for the hybrid LigEx method, a C/(Cu+Se) ratio of 0.10 was observed, with a thickness of ~100 nm.

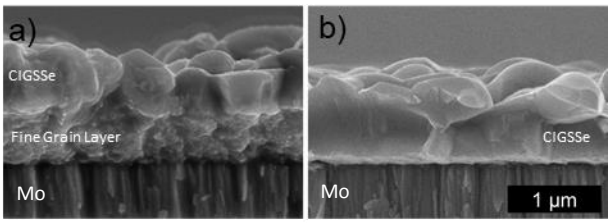

Figure 9. *SEM cross-sections of a selenized* ***a)*** *conventional non-ligand exchanged CIGS nanoparticle film, and* ***b)*** *hybrid ligand exchanged film at identical sodium content (10 nm NaF) and selenizaton conditions. The scale bar is the same for both images.*

Devices were prepared from both the conventional unexchanged and hybrid ligand exchanged methods. A notably higher efficiency of 12.0% was obtained as compared to the non-ligand exchange device with an efficiency of 9.2 %. As shown in Figure 10 and Table 1, nearly all device parameters have improved with the implementation of the hybrid ligand exchanged methods. Notably, we observe a 14.2% increase in J_{sc} which is attributed to the significantly enhanced grain growth of selenized hybrid ligand exchanged nanoparticle films as compared to the conventional unexchanged film, yielding thicker, high-quality grains of CIGSSe to absorb incident photons. Capacitance-voltage measurement of the hybrid ligand exchanged device revealed a majority carrier concentration of $1.30*10^{16}$ as shown in Figure S9. While promising initial efficiencies were obtained with selenized hybrid LigEx nanoparticle films, further optimization of selenization with thicker films may be a pathway to higher J_{sc}. Additionally, the incorporation of heavier alkali to improve V_{oc} and the incorporation of gallium grading to reduce interface recombination are both areas of future study to improve device efficiency and verify if such ligand exchange methods are more effective than the current record carbonaceous ligand containing nanoparticle films at reaching high efficiencies.[16] Nevertheless, removal of carbonaceous impurities represents a forward step in replicating the existing carbon-free, vacuum-based absorbers using highly scalable, solution processed colloidal nanoparticles.

Table 1. *Comparison of device characteristics between champion devices prepared from selenized conventional unexchanged nanoparticle films compared to selenized hybrid ligand exchange nanoparticle films. R_s, R_{sh}, and n (series resistance, shunt resistance, and diode ideality factor) were calculated using dark data and Hegedus and Shafarman's method.*[53]

	η (%)	V_{oc} (V)	J_{sc} (mA/cm^2)	FF (%)	R_s (Ω cm^2)	R_{sh} (Ω cm^2)	n
Unexchanged	9.2	0.57	26.0	62.1	0.9	554	1.71
Hybrid LigEx	12.0	0.60	29.7	67.5	1.00	605	1.59

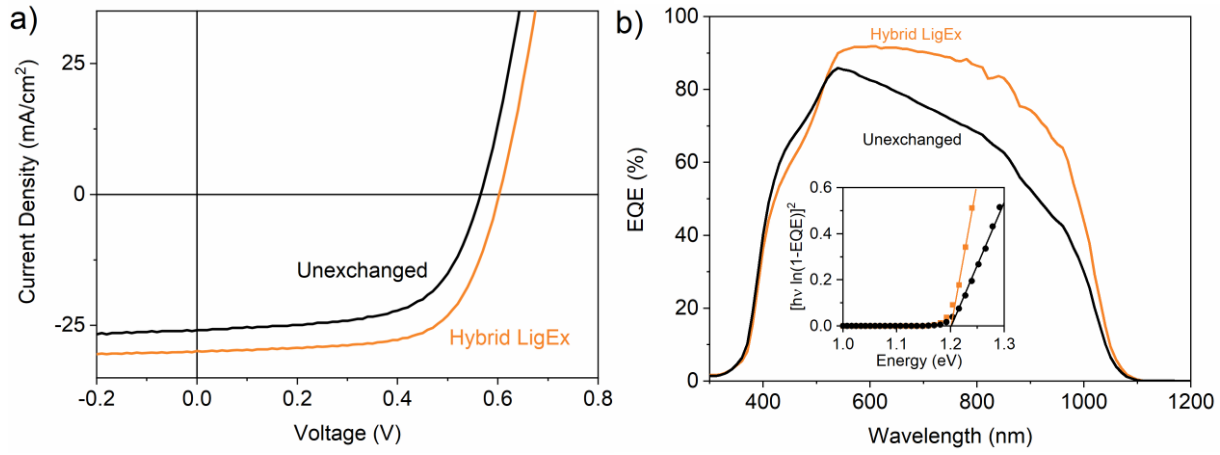

Figure 10. a) *J-V curve for devices prepared from selenized conventional unexchanged nanoparticle films compared to selenized hybrid ligand exchange nanoparticle films* ***b)*** *and corresponding EQE from each device.*

Conclusion

A rapid and exhaustive ligand exchange making use of sequential organic/inorganic exchanges was developed as a means to remove native oleylamine ligands and their resulting carbonaceous impurities in colloidal nanoparticle based $Cu(In,Ga)(S,Se)_2$ photovoltaics. Microwave-assisted solvothermal heating with pyridine enabled exposure of the nanoparticles to temperatures above oleylamine's desorption onset of 110°C-120°C and decreased the residence time needed for subsequent inorganic ligand exchange with the fairly aggressive species, diammonium sulfide. This hybrid organic/inorganic method prevented etching of the nanoparticle surface, decreased the total time needed for exchange, and improved the net removal of oleylamine as compared to each of its individual steps yielding greater than 98% removal of native ligands with negligible impact to nanoparticle stoichiometry. The hybrid ligand exchanged nanoparticles could be dispersed in stable and benign inks of dimethyl sufoxide at mass concentration exceeding 200 mg/mL, enabling scalable coating techniques such as blade coating. High quality, crack free, and ultra-smooth nanoparticle films were obtained from the hybrid ligand exchanged inks. Significantly improved selenization and grain growth was observed as compared to selenized films of conventionally prepared, non-ligand-exchanged nanoparticles. Subsequent devices showed that selenized hybrid ligand exchanged nanoparticle films yielded a substantial increase in power conversion efficiency over the non-ligand-exchanged control, reaching a champion total-area efficiency of 12.0%. The enhancements afforded by the hybrid ligand exchange over conventional methods demonstrates the merit of the developed methods for fabrication of high-quality solution-processed CIGSSe absorber layers.

Supporting Information

^{1}H-NMR comparison of alkene region single washed and four times washed CIGS nanoparticles, HAADF STEM image of as synthesized CIGS nanoparticles, mixture components and gas chromatogram from GC-MS of freeze-pump thawed oleyalmine mixture, ^{1}H-NMR of pyridine region from hybrid ligand exchanged nanoparticles, XRD and Raman of various ligand exchanges compared as-synthesized nanoparticles, optical micrograph and profilometry scan of film surface, Raman of a selenized hybrid ligand exchanged film's C-C region, STEM-EDS comparison of selenized hybrid ligand exchange film and conventionally prepared film, quantitative elemental distribution in fine grain layers, neighboring device parameters and averages for conventional and hybrid ligand exchanged devices, and N_{cv} versus width extracted from capacitance-voltage measurements

Acknowledgments

The authors would like to acknowledge funding from the National Science Foundation (NSF) under grants #1735282-NRT (SFEWS), #1534691-DMR (DMREF), and #10001536 (INFEWS). Research was carried out in part at the Center for Functional Nanomaterials, Brookhaven National Laboratory, which is supported by the U.S. Department of Energy, Office of Basic Energy Sciences, under Contract No. DE-SC0012704. The authors would also like to acknowledge Joseph Andler and Xianyi Hu for their assistance in preparing molybdenum coated soda-lime glass substrates, and Prof. Daniel Flaherty from the Department of Medicinal Chemistry and Molecular Pharmacology at Purdue University for allowing use of his Biotage Initiator microwave reactor. Additionally, the authors would like to acknowledge Dr. Huaping Mo from Purdue University's Interdepartmental NMR Facility for operating the NMR during the in-situ heat up ^{1}H-NMR experiment, Dr. Dmitry Zemlyanov from Purdue University's Birck Nanotechnology for running XPS data collection, Connie Bonham from the Purdue University Mass Spectrometry Center for running GC-MS, and Kyle Weidman for collecting HAADF STEM images on as-synthesized nanoparticles.

References

(1) Zhang, T.; Yang, Y.; Liu, D.; Tse, S. C.; Cao, W.; Feng, Z.; Chen, S.; Qian, L. High Efficiency Solution-Processed Thin-Film $Cu(In,Ga)(Se,S)_2$ Solar Cells. *Energy Environ. Sci.* **2016**, *9* (12), 3674–3681.

(2) Zhang, R.; Szczepaniak, S. M.; Carter, N. J.; Handwerker, C. A.; Agrawal, R. A Versatile Solution Route to Efficient $Cu_2ZnSn(S,Se)_4$ Thin-Film Solar Cells. *Chem. Mater.* **2015**, *27* (6), 2114–2120.

(3) Zhao, X.; Lu, M.; Koeper, M. J.; Agrawal, R. Solution-Processed Sulfur Depleted $Cu(In,Ga)Se_2$ Solar Cells Synthesized from a Monoamine–Dithiol Solvent Mixture. *J. Mater. Chem. A* **2016**, *4* (19), 7390–7397.

(4) Miskin, C. K.; Dubois-Camacho, A.; Reese, M. O.; Agrawal, R. A Direct Solution Deposition Approach to

CdTe Thin Films. *J. Mater. Chem. C* **2016**, *4*, 9167–9171.
(5) Murria, P.; Miskin, C. K.; Boyne, R.; Cain, L. T.; Yerabolu, R.; Zhang, R.; Wegener, E. C.; Miller, J. T.; Kenttämaa, H. I.; Agrawal, R. Speciation of CuCl and $CuCl_2$ Thiol-Amine Solutions and Characterization of Resulting Films: Implications for Semiconductor Device Fabrication. *Inorg. Chem.* **2017**, *56* (23), 14396–14407.
(6) Miskin, C. K.; Deshmukh, S. D.; Vasiraju, V.; Bock, K.; Mittal, G.; Dubois-Camacho, A.; Vaddiraju, S.; Agrawal, R. Lead Chalcogenide Nanoparticles and Their Size-Controlled Self-Assemblies for Thermoelectric and Photovoltaic Applications. *ACS Appl. Nano Mater.* **2019**, *2* (3), 1242–1252.
(7) Zhao, D.; Tian, Q.; Zhou, Z.; Wang, G.; Meng, Y.; Kou, D.; Zhou, W.; Pan, D.; Wu, S. Solution-Deposited Pure Selenide CIGSe Solar Cells from Elemental Cu, In, Ga, and Se. *J. Mater. Chem. A* **2015**, *3* (38), 19263–19267.
(8) Zhang, R.; Cho, S.; Lim, D. G.; Hu, X.; Stach, E. A.; Handwerker, C. A.; Agrawal, R. Metal–Metal Chalcogenide Molecular Precursors to Binary, Ternary, and Quaternary Metal Chalcogenide Thin Films for Electronic Devices. *Chem. Commun.* **2016**, *52* (28), 5007–5010.
(9) Zhao, X.; Deshmukh, S. D.; Rokke, D. J.; Zhang, G.; Wu, Z.; Miller, J. T.; Agrawal, R. Investigating Chemistry of Metal Dissolution in Amine–Thiol Mixtures and Exploiting It toward Benign Ink Formulation for Metal Chalcogenide Thin Films. *Chem. Mater.* **2019**, *31* (15), 5674–5682.
(10) Webber, D. H.; Buckley, J. J.; Antunez, P. D.; Brutchey, R. L. Facile Dissolution of Selenium and Tellurium in a Thiol–Amine Solvent Mixture under Ambient Conditions. *Chem. Sci.* **2014**, *5* (6), 2498.
(11) Walker, B. C.; Agrawal, R. Contamination-Free Solutions of Selenium in Amines for Nanoparticle Synthesis. *Chem. Commun.* **2014**, *50* (61), 8331–8334.
(12) Fan, Q.; Tian, Q.; Wang, H.; Zhao, F.; Kong, J.; Wu, S. Regulating the Starting Location of Front-Gradient Enabled Highly Efficient $Cu(In,Ga)Se_2$ Solar Cells via a Facile Thiol–Amine Solution Approach. *J. Mater. Chem. A* **2018**, *6* (9), 4095–4101.
(13) Uhl, A. R.; Katahara, J. K.; Hillhouse, H. W. Molecular-Ink Route to 13.0% Efficient Low-Bandgap $CuIn(S,Se)_2$ and 14.7% Efficient $Cu(In,Ga)(S,Se)_2$ Solar Cells. *Energy Environ. Sci.* **2016**, *9* (1), 130–134.
(14) Clark, J. A.; Murray, A.; Lee, J. M.; Autrey, T. S.; Collord, A. D.; Hillhouse, H. W. Complexation Chemistry in N,N-Dimethylformamide-Based Molecular Inks for Chalcogenide Semiconductors and Photovoltaic Devices. *J. Am. Chem. Soc.* **2019**, *141* (1), 298–308.
(15) Jiang, J.; Giridharagopal, R.; Jedlicka, E.; Sun, K.; Yu, S.; Wu, S.; Gong, Y.; Yan, W.; Ginger, D. S.; Green, M. A.; Hao, X.; Huang, W.; Xin, H. Highly Efficient Copper-Rich Chalcopyrite Solar Cells from DMF Molecular Solution. *Nano Energy* **2020**, *69*, 104438.
(16) McLeod, S. M.; Hages, C. J.; Carter, N. J.; Agrawal, R. Synthesis and Characterization of 15% Efficient CIGSSe Solar Cells from Nanoparticle Inks. *Prog. Photovoltaics Res. Appl.* **2015**, *23* (11), 1550–1556.
(17) Ellis, R. G.; Vak, D.; Chesman, A. S. R.; Agrawal, R. Slot Die Coating of CIGS Nanoparticle Inks for Scalable Solution Processed Photovoltaics. In *46th IEEE PVSC* **2019**, 1830–1833
(18) Guo, Q.; Ford, G. M.; Agrawal, R.; Hillhouse, H. W. Ink Formulation and Low-Temperature Incorporation of Sodium to Yield 12% Efficient $Cu(In ,Ga)(S,Se)_2$ Solar Cells from Sulfide Nanocrystal Inks. *Prog. Photovoltaics Res. Appl.* **2013**, *21*, 64–71.
(19) McLeod, S.; Alruqobah, E.; Agrawal, R. Liquid Assisted Grain Growth in Solution Processed $Cu(In,Ga)(S,Se)_2$. *Sol. Energy Mater. Sol. Cells* **2019**, *195*, 12–23.
(20) Martin, T. R.; Katahara, J. K.; Bucherl, C. N.; Krueger, B. W.; Hillhouse, H. W.; Luscombe, C. K. Nanoparticle Ligands and Pyrolized Graphitic Carbon in CZTSSe Photovoltaic Devices. *Chem. Mater.* **2016**, *28* (1), 135–145.
(21) Rehan, S.; Kim, K. Y.; Han, J.; Eo, Y.-J.; Gwak, J.; Ahn, S. K.; Yun, J. H.; Yoon, K.; Cho, A.; Ahn, S. Carbon-Impurity Affected Depth Elemental Distribution in Solution-Processed Inorganic Thin Films for Solar Cell Application. *ACS Appl. Mater. Interfaces* **2016**, *8* (8), 5261–5272.
(22) van Embden, J.; Chesman, A. S. R.; Jasieniak, J. J. The Heat-Up Synthesis of Colloidal Nanocrystals. *Chem. Mater.* **2015**, *27* (7), 2246–2285.
(23) Coughlan, C.; Ibáñez, M.; Dobrozhan, O.; Singh, A.; Cabot, A.; Ryan, K. M. Compound Copper Chalcogenide Nanocrystals. *Chem. Rev.* **2017**, *117* (9), 5865–6109.
(24) Hages, C. J.; Koeper, M. J.; Miskin, C. K.; Brew, K. W.; Agrawal, R. Controlled Grain Growth for High Performance Nanoparticle-Based Kesterite Solar Cells. *Chem. Mater.* **2016**, *28* (21), 7703–7714.
(25) Wu, W.; Cao, Y.; Caspar, J. V.; Guo, Q.; Johnson, L. K.; Malajovich, I.; Rosenfeld, H. D.; Choudhury, K. R. Studies of the Fine-Grain Sub-Layer in the Printed CZTSSe Photovoltaic Devices. *J. Mater. Chem. C* **2014**, *2* (19), 3777–3781.

(26) Boles, M. A.; Ling, D.; Hyeon, T.; Talapin, D. V. The Surface Science of Nanocrystals. *Nat. Mater.* **2016**, *15* (2), 141–153.
(27) Lokteva, I.; Radychev, N.; Witt, F.; Borchert, H.; Parisi, J.; Kolny-Olesiak, J. Surface Treatment of CdSe Nanoparticles for Application in Hybrid Solar Cells: The Effect of Multiple Ligand Exchange with Pyridine. *J. Phys. Chem. C* **2010**, *114* (29), 12784–12791.
(28) Anderson, N. C.; Hendricks, M. P.; Choi, J. J.; Owen, J. S. Ligand Exchange and the Stoichiometry of Metal Chalcogenide Nanocrystals: Spectroscopic Observation of Facile Metal-Carboxylate Displacement and Binding. *J. Am. Chem. Soc.* **2013**, *135* (49), 18536–18548.
(29) Panthani, M. G.; Kurley, J. M.; Crisp, R. W.; Dietz, T. C.; Ezzyat, T.; Luther, J. M.; Talapin, D. V. High Efficiency Solution Processed Sintered CdTe Nanocrystal Solar Cells: The Role of Interfaces. *Nano Lett.* **2014**, *14* (2), 670–675.
(30) Munro, A. M.; Bardecker, J. A.; Liu, M. S.; Cheng, Y. J.; Niu, Y. H.; Plante, I. J. La; Jen, A. K. Y.; Ginger, D. S. Colloidal CdSe Quantum Dot Electroluminescence: Ligands and Light-Emitting Diodes. *Microchim. Acta* **2008**, *160* (3), 345–350.
(31) Dai, M. Q.; Yung, L. Y. L. Ethylenediamine-Assisted Ligand Exchange and Phase Transfer of Oleophilic Quantum Dots: Stripping of Original Ligands and Preservation of Photoluminescence. *Chem. Mater.* **2013**, *25* (11), 2193–2201.
(32) Luther, J. M.; Law, M.; Song, Q.; Perkins, C. L.; Beard, M. C.; Nozik, A. J. Structural, Optical, and Electrical Properties of Self-Assembled Films of PbSe Nanocrystals Treated with 1,2-Ethanedithiol. *ACS Nano* **2008**, *2* (2), 271–280.
(33) Webber, D. H.; Brutchey, R. L. Ligand Exchange on Colloidal CdSe Nanocrystals Using Thermally Labile Tert -Butylthiol for Improved Photocurrent in Nanocrystal Films. *J. Am. Chem. Soc.* **2012**, *134* (2), 1085–1092.
(34) Brown, P. R.; Kim, D.; Lunt, R. R.; Zhao, N.; Bawendi, M. G.; Grossman, J. C.; Bulović, V. Energy Level Modification in Lead Sulfide Quantum Dot Thin Films through Ligand Exchange. *ACS Nano* **2014**, *8* (6), 5863–5872.
(35) Nag, A.; Kovalenko, M. V; Lee, J.; Liu, W.; Spokoyny, B.; Talapin, D. V. Metal-Free Inorganic Ligands for Colloidal Nanocrystals: S^{2-}, HS^{-}, Se^{2-}, HSe^{-}, Te^{2-}, HTe^{-}, TeS_3^{2-}, OH^{-}, and NH_2^{-} as Surface Ligands. *J. Am. Chem. Soc.* **2011**, *133* (27), 10612–10620.
(36) Korala, L.; Braun, M. B.; Kephart, J. M.; Tregillus, Z.; Prieto, A. L. Ligand-Exchanged CZTS Nanocrystal Thin Films: Does Nanocrystal Surface Passivation Effectively Improve Photovoltaic Performance? *Chem. Mater.* **2017**, *29* (16), 6621–6629.
(37) Dierick, R.; Van den Broeck, F.; De Nolf, K.; Zhao, Q.; Vantomme, A.; Martins, J. C.; Hens, Z. Surface Chemistry of $CuInS_2$ Colloidal Nanocrystals, Tight Binding of L-Type Ligands. *Chem. Mater.* **2014**, *26* (20), 5950–5957.
(38) Houck, D. W.; Korgel, B. A. Facile Exchange of Tightly Bonded L-Type Oleylamine and Diphenylphosphine Ligands on Copper Indium Diselenide Nanocrystals Mediated by Molecular Iodine. *Chem. Mater.* **2018**, *30* (22), 8359–8367.
(39) Dilena, E.; Xie, Y.; Brescia, R.; Prato, M.; Maserati, L.; Krahne, R.; Paolella, A.; Bertoni, G.; Povia, M.; Moreels, I.; Manna, L. $CuIn_xGa_{1-x}S_2$ Nanocrystals with Tunable Composition and Band Gap Synthesized via a Phosphine-Free and Scalable Procedure. *Chem. Mater.* **2013**, *25* (15), 3180–3187.
(40) Deshmukh, S. D.; Ellis, R. G.; Sutandar, D. S.; Rokke, D. J.; Agrawal, R. Versatile Colloidal Syntheses of Metal Chalcogenide Nanoparticles from Elemental Precursors Using Amine-Thiol Chemistry. *Chem. Mater.* **2019**, *31* (21), 9087–9097.
(41) Niederberger, M.; Garnweitner, G.; Buha, J.; Polleux, J.; Ba, J.; Pinna, N. Nonaqueous Synthesis of Metal Oxide Nanoparticles:Review and Indium Oxide as Case Study for the Dependence of Particle Morphology on Precursors and Solvents. *J. Sol-Gel Sci. Technol.* **2006**, *40* (2–3), 259–266.
(42) Fritzinger, B.; Moreels, I.; Lommens, P.; Koole, R.; Hens, Z.; Martins, J. C. In Situ Observation of Rapid Ligand Exchange in Colloidal Nanocrystal Suspensions Using Transfer NOE Nuclear Magnetic Resonance Spectroscopy. *J. Am. Chem. Soc.* **2009**, *131* (8), 3024–3032.
(43) Duchatelet, A.; Sidali, T.; Loones, N.; Savidand, G.; Chassaing, E.; Lincot, D. 12.4% Efficient $Cu(In,Ga)Se_2$ Solar Cell Prepared from One Step Electrodeposited Cu-In-Ga Oxide Precursor Layer. *Sol. Energy Mater. Sol. Cells* **2013**, *119*, 241–245.
(44) Uhl, A. R.; Fuchs, P.; Rieger, A.; Pianezzi, F.; Sutter-Fella, C. M.; Kranz, L.; Keller, D.; Hagendorfer, H.; Romanyuk, Y. E.; Lamattina, F.; Yoon, S.; Karvonen, L.; Magorian-Friedlmeier, T.; Ahlswede, E.; VanGenechten, D.; Stassin, F.; Tiwari, A. N. Liquid-Selenium-Enhanced Grain Growth of Nanoparticle

Precursor Layers for $CuInSe_2$ Solar Cell Absorbers. *Prog. Photovoltaics Res. Appl.* **2015**, *23* (9), 1110–1119.
(45) Rockett, A.; Britt, J. S.; Gillespie, T.; Marshall, C.; Al Jassim, M. M.; Hasoon, F.; Matson, R.; Basol, B. Na in Selenized Cu(In,Ga)Se_2 on Na-Containing and Na-Free Glasses: Distribution, Grain Structure, and Device Performances. *Thin Solid Films* **2000**, *372* (1), 212–217.
(46) Dierick, R.; Capon, B.; Damm, H.; Flamee, S.; Arickx, P.; Bruneel, E.; Van Genechten, D.; Van Bael, M.; Hardy, A.; Detavernier, C.; Hens, Z. Annealing of Sulfide Stabilized Colloidal Semiconductor Nanocrystals. *J. Mater. Chem. C* **2014**, *2* (1), 178–183.
(47) Guo, J.; Wang, X.; Zhou, W. H.; Chang, Z. X.; Zhou, Z. J.; Wu, S. X. Efficiency Enhancement of Dye-Sensitized Solar Cells (DSSCs) Using Ligand Exchanged $CuInS_2$ NCs as Counter Electrode Materials. *RSC Adv.* **2013**, *3* (34), 14731–14736.
(48) Hassinen, A.; Moreels, I.; De Nolf, K.; Smet, P. F.; Martins, J. C.; Hens, Z. Short-Chain Alcohols Strip X-Type Ligands and Quench the Luminescence of PbSe and CdSe Quantum Dots, Acetonitrile Does Not. *J. Am. Chem. Soc.* **2012**, *134* (51), 20705–20712.
(49) Khatri, I.; Fukai, H.; Yamaguchi, H.; Sugiyama, M.; Nakada, T. Effect of Potassium Fluoride Post-Deposition Treatment on Cu(In,Ga)Se_2 Thin Films and Solar Cells Fabricated onto Sodalime Glass Substrates. *Sol. Energy Mater. Sol. Cells* **2016**, *155*, 280–287.
(50) Barbé, J.; Eid, J.; Ahlswede, E.; Spiering, S.; Powalla, M.; Agrawal, R.; Del Gobbo, S. Inkjet Printed Cu(In,Ga)S_2 Nanoparticles for Low-Cost Solar Cells. *J. Nanoparticle Res.* **2016**, *18* (12), 379.
(51) Harvey, T. B.; Bonafé, F.; Updegrave, T.; Voggu, V. R.; Thomas, C.; Kamarajugadda, S. C.; Stolle, C. J.; Pernik, D.; Du, J.; Korgel, B. A. Uniform Selenization of Crack-Free Films of Cu(In,Ga)Se_2 Nanocrystals. *ACS Appl. Energy Mater.* **2019**, *2* (1), 736–742.
(52) Perlich, J.; Metwalli, E.; Schulz, L.; Georgii, R.; Müller-Buschbaum, P. Solvent Content in Thin Spin-Coated Polystyrene Homopolymer Films. *Macromolecules* **2009**, *42* (1), 337–344.
(53) Hegedus, S. S.; Shafarman, W. N. Thin-Film Solar Cells: Device Measurements and Analysis. *Prog. Photovoltaics Res. Appl.* **2004**, *12* (23), 155–176.

Table of Contents Graphic

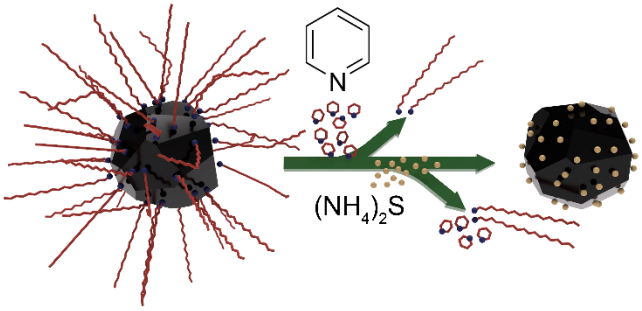

Supporting Information

Hybrid Ligand Exchange of $Cu(In,Ga)S_2$ Nanoparticles for Carbon Impurity Removal in Solution Processed Photovoltaics

Ryan G. Ellis, Jonathan W. Turnley, David J. Rokke, Jacob P. Fields, Essam H. AlRuqobah, Swapnil D. Deshmukh, Kim Kisslinger [‡] and Rakesh Agrawal*

Davidson School of Chemical Engineering, Purdue University, West Lafayette, IN 47907, USA
[‡] Center for Functional Nanomaterials, Brookhaven National Laboratory, Upton, NY 11973, USA

*Corresponding author: agrawalr@purdue.edu

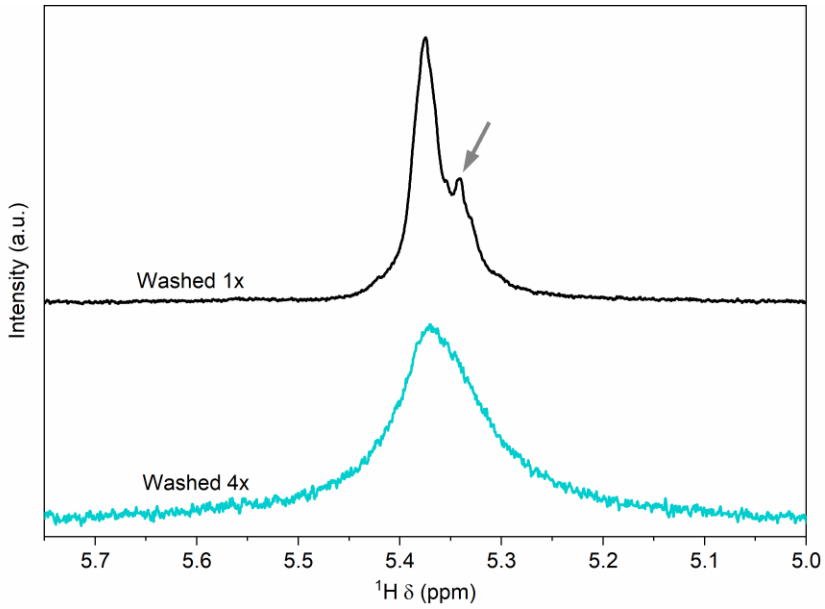

Figure S1. *^{1}H-NMR of the alkene proton resonance of oleylamine capped CIGS nanoparticles after being washed (as described in the experimental section) for one and four cycles. Arrow shows sharp resonance of free oleylamine, demonstrating underpurification. Chloroform-D was used as a deuterated solvent.*

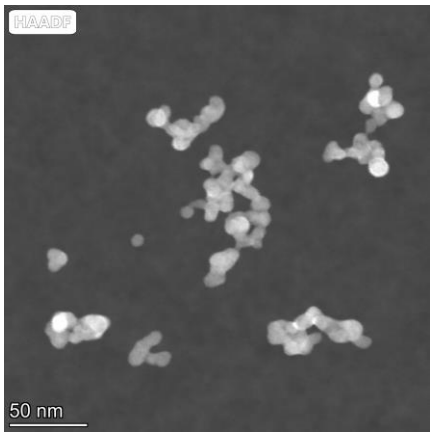

Figure S2. *HAADF STEM image of as-synthesized CIGS nanoparticles with a 90-minute reaction time.*

Table S1. *GC-MS mixture composition of technical grade oleylamine after freeze-pump-thaw degassing, species identified via MS.*

Molecule	% Compound
Oleylamine	82.7
Hexadecenylamine	4.6
Octadecylamine	4.1
Hexadecylamine	3.6
Trace Components (n-octylformamide, oleylanitrile, column bleed)	5

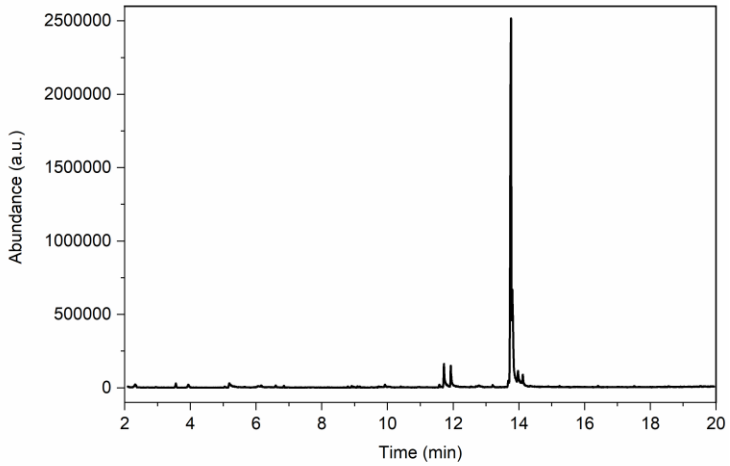

Figure S3. *Gas chromatogram of the technical grade oleylamine in CH_2Cl_2*

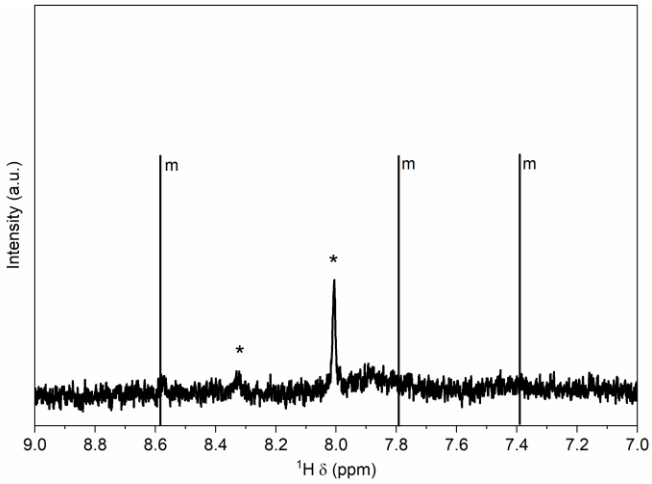

Figure S4. *^{1}H-NMR after hybrid ligand exchange showing no residual pyridine content (* denote trace impurities and black lines indicate the centers of the multiplet (m) peaks of pyridine in DMSO-D_6). DMSO-D_6 was used as a deuterated solvent.*

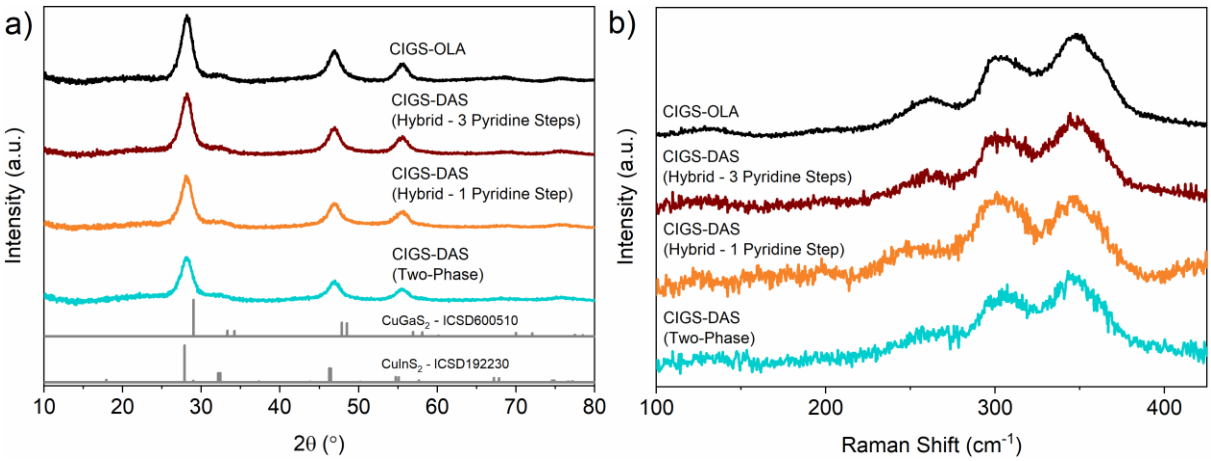

Figure S5. a) *XRD and* ***b)*** *Raman of single step and hybrid ligand exchanged films with 1 and 3 pyridine cycles.*

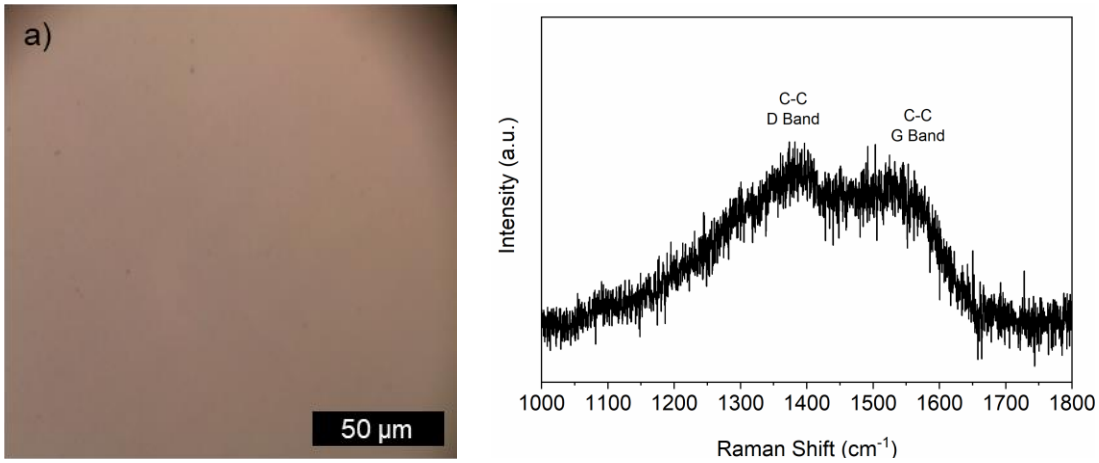

Figure S6. a) *Optical microscope image of coated ligand exchanged film and* ***b)*** *profilometry demonstrating low surface roughness and lack of microcracks.*

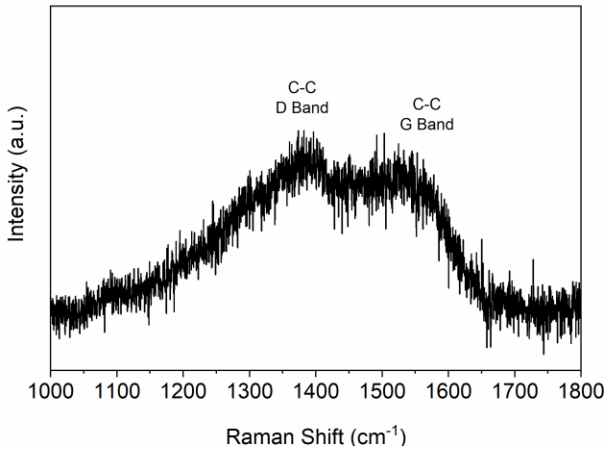

Figure S7. *Raman spectrum of a thin selenized hybrid LigEx nanoparticle film showing trace graphitic carbon content persisting in the absorber.*

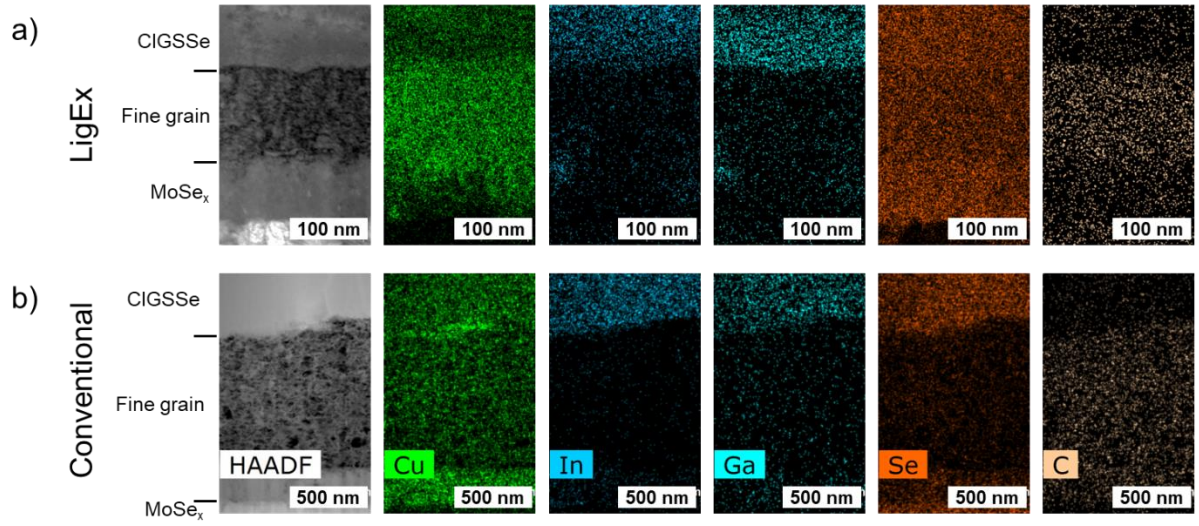

Figure S8. *STEM-EDS of residual unsintered layer on a* ***a)*** *hybrid ligand exchanged film* ***b)*** *conventional non-ligand-exchanged film. Note the difference in scale bars between images.*

Table S2. *Atomic percent of various species present in the fine grain layer for both hybrid LigEx films and conventional films.*

Atom	LigEx (at%)	Conventional (at%)
Cu	41.10	23.02
In	1.21	0.60
Ga	1.24	1.81
S	2.40	2.34
Se	35.83	16.12
C	8.11	34.35
O	2.14	14.07
Na	3.63	5.78
Mo	4.34	1.91

The conventional films have a predominantly carbon based fine grain layer with significantly higher carbon content than the hybrid LigEx film. Additionally, a "sponge" like morphology can be observed for the conventional film's carbon based fine grain layer whereas the for the hybrid LigEx film, a more nanocrystalline appearance is observed. A slight increase in carbon content as compared to the bulk background is observed for the hybrid LigEx film (possibly due to the ~1.4% native ligand remaining as well as potentially decomposed entrained solvent). However, the residual unsintered layer is composed almost entirely of copper and selenium, devoid of gallium and indium. As mentioned in the text, a C/(Cu+Se) ratio of 0.10 is observed for a ~100 nm thick fine grain whereas for the conventional film a C/(Cu+Se) ratio of 0.88 is observed for a substantially thicker layer. For the hybrid LigEx, this suggests that this unincorporated layer is a function of the selenization reaction mechanism as opposed to carbon entrainment. We hypothesize that the similar ratio of copper and selenium, or a CuSe like material, is the result of the high selenium vapor pressure present during selenization. This may cause copper to maintain a +2 oxidation state, thereby preventing its incorporation into the $Cu(In,Ga)(S,Se)_2$ lattice in the +1 oxidation state. More fine control of selenium may be needed to generate fully laterally spanning grains using techniques such as flow RTP, where selenium temperature can

be controlled independently of the substrate as is shown in previous reports. However, existing results show promise, nearly removing unsintered/carbon residue layers and significantly improving grain growth due to the absence of carbon impurity.

Table S3. Device parameters of the cells on the same film as the champion hybrid LigEx device (Cell 2). Device characteristics reported from total area which was determined from image analysis (A = 0.451, 0.458, and 0.454 cm^2 for cells 1,2 and 3 respectively).

	η (%)	**V_{oc} (V)**	**J_{sc} (mA/cm^2)**	**FF (%)**	**R_s (Ω cm^2)**	**R_{sh} (Ω cm^2)**	**n**
1	11.8	0.60	29.7	66.1	1.22	576	1.55
2	12.0	0.60	29.7	67.5	1.00	605	1.59
3	11.9	0.60	29.5	67.1	0.93	502	1.48
Average	11.9	0.60	29.6	66.9	1.05	561	1.54

Table S4. Device parameters of the cells on the same film as the conventional device (Cell 1 parameters used in manuscript). Device characteristics reported from total area which was determined from image analysis (A = 0.510, 0.514, and 0.515 cm^2 for cells 1, 2 and 3 respectively).

	η (%)	**V_{oc} (V)**	**J_{sc} (mA/cm^2)**	**FF (%)**	**R_s (Ω cm^2)**	**R_{sh} (Ω cm^2)**	**n**
1	9.2	0.57	26.0	62.1	0.9	554	1.71
2	9.0	0.58	25.8	60.3	1.04	476	1.58
3	8.3	0.57	23.1	62.8	1.13	297	1.55
Average	8.8	0.57	25.0	61.7	1.02	442	1.61

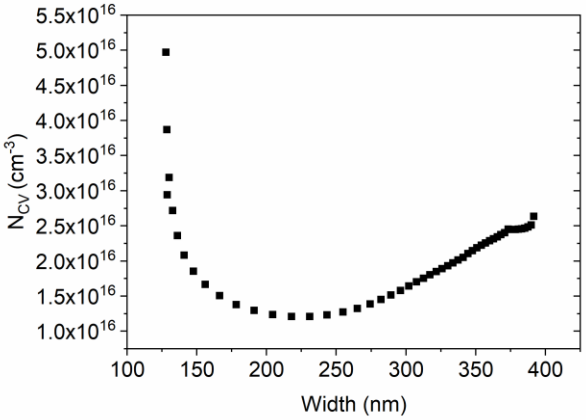

Figure S9. *N_{CV} versus width extracted from capacitance-voltage measurements on cell 3 for the hybrid LigEx device.*